JASA ARTICLE

Use of simulated data to explore the application of optical coherence tomography for classifying middle-ear pathologies

Marzieh Golabbakhsh and W. Robert J. Funnell[a)]
Department of BioMedical Engineering, McGill University, Montréal, Québec, Canada

ABSTRACT:
Optical coherence tomography (OCT) vibrometry is a non-invasive tool for functional imaging of the middle ear. It provides spatially resolved vibrational responses and also anatomical images of the same ear. Our objective here was to explore the potential of OCT vibration measurements at the incus, as well as at the umbo, to distinguish among middle-ear disorders. Our approach was to build finite-element models of normal and pathological ears, generate large amounts of synthetic data, and then classify the simulated data into normal and pathological groups using a decision tree based on features extracted from simulated vibration magnitudes. We could distinguish between normal ears and ears with incudomallear joint (IMJ) disarticulation or stapes fixation, with the sensitivity and specificity both being 1.0; distinguish between stapes fixation and IMJ disarticulation with a sensitivity of 0.900 and a specificity of 0.889; and distinguish ears with ISJ disarticulation from normal ears with a sensitivity of 0.784 and a specificity of 0.872. Less extreme pathologies were also simulated. The results suggest that the vibration measurements within the middle ear that can be provided by OCT (e.g., at the incus) may be very valuable for diagnosis.
 https://doi.org/10.1121/10.0022051
(Received 29 May 2023; revised 5 October 2023; accepted 8 October 2023; published online 2 November 2023)
[Editor: Julien Meaud] Pages: 2790–2799

I. INTRODUCTION

Hearing loss is very prevalent, affecting more than 1.5 $\times$ 10^9 people globally, including almost two-thirds of persons over the age of 60 years (World Health Organization, 2021). Unaddressed hearing loss has many negative effects, and leads to high costs for health-care systems. New technologies that improve diagnostic accuracy and efficacy are sought.

Optical coherence tomography (OCT) vibrometry is a promising tool for functional imaging of the middle ear. It is based on low-coherence interferometry, typically with near-infrared light. It is a non-invasive means of obtaining spatially resolved vibrational responses and also anatomical images. Such information can potentially improve diagnostic sensitivity and specificity as compared to current approaches. A recent technical review by Ramier *et al.* (2018) describes the history of OCT for imaging the middle ear and inner ear. Most middle-ear disorders involve fixations or discontinuities at specific locations within the ossicular chain (e.g., Park *et al.*, 2014) and the ability to measure both function and anatomy will help in finding the precise location of the pathology.

A computational model can simulate how different parts of the middle ear behave mechanically under different loads. Such models can be used to simulate pathological conditions and to assess how the pathologies will affect middle-ear function. In finite-element (FE) models in particular (e.g., Daniel *et al.*, 2001; Huber *et al.*, 2003; Dai *et al.*, 2007), pathologies can be simulated by changing the material properties and boundary conditions of the model in ways that are directly related to the nature of the pathology. For example, increasing the stiffness parameter of the stapedial annular ligament (SAL) can be used to simulate stapes fixation. We can also add or remove material or otherwise modify parts of the models.

Pathologies at different locations can best be characterized by considering vibrations at multiple points in the ossicular chain. While laser Doppler vibrometry (LDV) measurements can be made at middle-ear locations behind the tympanic membrane (TM) in cadaver temporal bones, in patients, they can only be made at the level of the TM, and not deeper. Recently, OCT Doppler vibrometry (OCT-DV) has been able to provide deep vibration measurements in temporal bones and patients. For example, MacDougall *et al.* (2019) used OCT vibration measurements in patients to distinguish patients with stapes fixation from normal controls and they concluded that "OCT-DV alone can achieve sensitivity and specificity higher than combined audiometry and LDV." [Another issue with LDV is its dependence on the presence of a naturally reflective bright spot on the TM, the light reflex, which is missing in some patients because of normal anatomical differences (Merchant, 2014, p. 49).]

In a previous study (Golabbakhsh *et al.*, 2023), we reported three FE models that were built based on geometries obtained from micro-scale X-ray computed tomography (microCT) images of normal middle ears and validated

[a)]Also at: Department of Otolaryngology–Head & Neck Surgery, McGill University, Montréal, Québec, Canada. Email: robert.funnell@mcgill.ca

https://doi.org/10.1121/10.0022051

against OCT vibration measurements in the same ears. Our objective here is to use one of those models to explore the feasibility of using OCT vibration measurements at the umbo and incus to distinguish among various disorders. We do this by modifying the model to represent pathological ears, randomly generating large amounts of normal and pathological synthetic data; and then using a decision tree to classify the synthetic data into groups of normal ears and ears with different disorders.

II. METHODS

One of the three FE middle-ear models (2017-2) of Golabbakhsh *et al.* (2023) was used in this study (see Funnell and Golabbakhsh, 2022 for the model definition). We had microCT and OCT data for the same ear, recorded at Dalhousie University in Halifax, Canada. As described in Golabbakhsh *et al.* (2023), the microCT images were segmented manually using locally developed software (audilab.bme.mcgill.ca/sw), which was also used to specify the material properties, boundary conditions, and acoustic loads, and for the generation of triangulated surfaces. The volume mesh generation was done with Gmsh (Geuzaine and Remacle, 2009). The model (Fig. 1) included the following separate structures: pars tensa (PT) and pars flaccida (PF) of the TM, TM-malleus connection (TMMC), malleus, incus, stapes, incudomallear joint (IMJ), and incudostapedial joint (ISJ). The SAL was represented by discrete springs. The value of the stiffness of the SAL was taken from Kwacz *et al.* (2015). Given that the highest frequency of interest was 3 kHz, the anterior mallear ligament (AML) and posterior incudal ligament (PIL) were not modelled. Instead, we implemented a practically fixed axis of rotation by using very stiff springs. Experiments have shown that the axis of rotation is almost fixed at low frequencies (Gundersen and Høgmoenm, 1976) so the results up to 3 kHz are not expected to change much. Since the contrast of the microCT images was inadequate for segmentation of soft-tissue structures, histological images of human ears were used as a supplement. Detailed specifications of the FE model were given in Golabbakhsh *et al.* (2023).

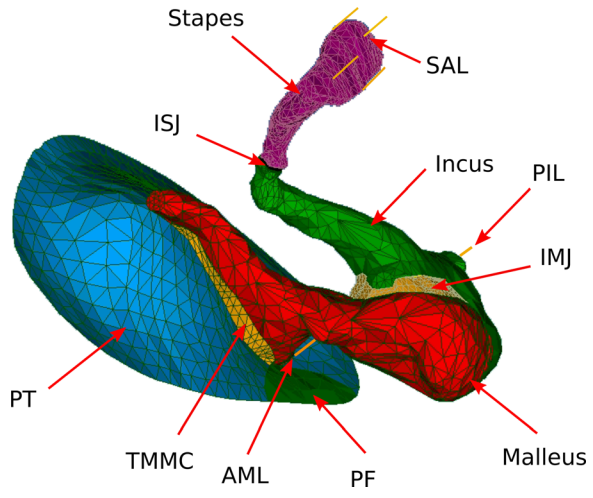

FIG. 1. (Color online) FE model of the human ear. PT, pars tensa; PF, pars flaccida; TMMC, TM-malleus connection; IMJ, incudomallear joint; ISJ, incudostapedial joint; SAL, stapedial annular ligament; AML, anterior mallear ligament; PIL, posterior incudal ligament. Straight yellow lines indicate the attachment points of the SAL, AML, and PIL.

Code_Aster 14.6 (code-aster.org) was used for FE analysis. We used the high-performance computing resources of the Digital Research Alliance of Canada. In particular, we used Narval, a heterogeneous multi-purpose cluster consisting of a mix of AMD EPYC Rome and Milan processors (Advanced Micro Devices, Inc., Santa Clara, CA) connected by a Mellanox HDR InfiniBand network (NVIDIA, Santa Clara, CA) (https://docs.alliancecan.ca/wiki/Narval/en). Each 64-core Rome processor can theoretically perform up to about 2.5×10^{12} double-precision floating-point operations (FLOPs) per second. [However, interpreting the performance of modern processors in terms of FLOP/s is not straightforward (e.g., Dolbeau, 2018).] We ran multiple simulations in Code_Aster simultaneously using Slurm (www.schedmd.com) job arrays, each containing 1000 jobs, the maximum number allowed for one job array on Narval. Each job in the job array ran the simulation for one combination of model parameters. We specified a maximum of 20 min for each job array, one central processing unit (CPU) per task, and 1 GB of memory per CPU. Each job takes about 20 to 30 s of wall-clock time.

The previous FE model of a normal ear was altered by changing the material properties and boundary conditions linked to the causes of three different middle-ear pathologies: stapes fixation, disarticulation of the ISJ, and disarticulation of the IMJ. We took the parameters related to each pathology from Sackmann *et al.* (2022). For the simulation of stapes fixation, the baseline stiffness of the SAL was set to 1000 times the value for the normal case. For the simulation of disarticulation of each of the joints (IMJ and ISJ), the stiffness and the loss ratio of the joint were both set to zero.

We created synthetic data incorporating inter-ear variability by varying eight parameters of the model for the normal case and the pathological cases: thickness and Young's modulus of PT, Young's modulus of IMJ and ISJ, stiffness of SAL, loss ratio of soft tissues, and cochlear damping. For the loss ratio and cochlear damping, we randomly took either the baseline value or a value that was multiplied or divided by a factor of 1.5 or 1.2. To set the other parameters for each simulation, we used the same method but factors of 3 and 1.5 were used. Table I shows the baseline values of the parameters for the normal and pathological cases.

The OCT vibration measurements in Golabbakhsh *et al.* (2023) were made only at 500, 1000, and 2000 Hz. In this study, however, we explored more frequencies, calculating simulated displacement magnitudes at 11 frequencies with an equal interval of 250 Hz, from 500 to 3000 Hz.

III. RESULTS

Figure 2 shows violin plots of the displacement magnitude at the umbo at frequencies from 500 Hz to 3 kHz, for

TABLE I. Model material properties. (Values in parentheses refer to less extreme versions of the pathologies, as discussed in the text.)

Parameter	Baseline model	IMJ disarticulation	ISJ disarticulation	Stapes fixation
PT Young's modulus	10 MPa	—	—	—
PT thickness	40 μm	—	—	—
IMJ Young's modulus	7 MPa	0 (7 kPa)	—	—
IMJ loss ratio	0.2	0	—	—
ISJ Young's modulus	6 MPa	—	0	—
ISJ loss ratio	0.2	—	0	—
TMMC Young's modulus	2 MPa	—	—	—
SAL stiffness	120 N/m	—	—	120 000 N/m (12 000)
Loss ratio	0.2	—	—	—
Cochlear damping	0.05	—	—	—

normal ears and for the three different disorders, along with values of displacement magnitude at the umbo from previous *in vivo* studies (Rosowski *et al.*, 2012; Merchant, 2014; Farahmand *et al.*, 2016; Masud, 2020) and from the temporal-bone study of Cheng *et al.* (2021), which all included frequencies from 300 to 6000 Hz. The curves for baseline models are presented on top of the violin plots. The baseline models have parameter values in the middles of their ranges of variation but their displacements are not always in the middles of the violin plots, reflecting the bias noted by Ebrahimian *et al.* (2023b). In addition, the plots are not unimodal, which suggests that there are parameter interactions in the model. The parameters vary independently and any interactions among the parameters will be reflected in the distributions of the simulated data. We can see that the magnitudes are higher for the *in vivo* measurements than for our simulation results, possibly because our normal model was validated against OCT measurements in temporal bones. The normal temporal-bone measurements of Cheng *et al.* (2021) that are presented in Fig. 2(a) are consistent with our baseline model results. The plot shows that the frequency responses of our baseline model fall faster at high frequencies compared with the experimental data. As discussed in Golabbakhsh *et al.* (2023), we think this might be because we have not modelled the suspensory ligaments and instead have a fixed axis of rotation.

In spite of the differences in the displacements themselves, the displacement changes due to the simulated pathologies in our results are in qualitative agreement with experimentally measured changes in normal subjects and patients. For ossicular discontinuity, Merchant (2014, Fig. 2.8a) reported an increase in the umbo displacement magnitude below 1 kHz by factors of about 2 to 15 in five of six patient ears, but a decrease by a factor of about 2.5 for the one ear that had a "round-shaped tympanogram, consistent with a middle-ear system stiffer than normal." Farahmand *et al.* [2016, Fig. 2(b)] reported that 21 of 29 patients with ossicular discontinuity showed values larger than normal by a factor of between 3 and 4 at frequencies below 1 kHz. In our simulated data, we see an increase by more than a factor of 5 below 1 kHz for ISJ and IMJ disarticulation [Figs. 2(b) and 2(c)], but there is little change at higher frequencies. For stapes fixation, Merchant (2014, Fig. 2.7a) reported a decrease by a factor of 5 to 8 for the displacement magnitude at frequencies below 1 kHz in four of five patient ears, but an increase by a factor of around 4 for the remaining ear (which had a normal tympanogram). We see a decrease by factors of about 10 for our models of stapes fixation below 2 kHz [Fig. 2(d)].

Figure 3 shows plots of umbo vibration magnitudes against the vibration magnitudes of the long process of the incus at six different frequencies (500 Hz, 750 Hz, 1 kHz, 1.5 kHz, 2 kHz, 3 kHz) for 1000 simulations for normal ears and 1000 simulations for each category of pathological ears, to give an overview of the simulation results. Each panel shows 4000 simulation results (1000 simulations for each middle-ear case). (At 500 and 750 Hz for stapes fixation, the umbo and incus displacements were both very small for all of the simulations; therefore, the results overlap substantionally, which is why there seem to be only a few stars.) The incus-vs-umbo displacement plots for different pathological conditions appear as roughly linear for each condition, with a different slope in each case. We see that when the frequency increases, the categories become more scattered but are still separable to some extent. As discussed below, the variability at the higher frequencies is probably a result of the increasing complexity of the three-dimensional (3D) motions of the middle ear and the increasing irregularity of the responses in the frequency domain (e.g., Decraemer and Khanna, 2004; Maftoon *et al.*, 2015). We concluded from these plots that there was potentially useful diagnostic information in the ratio of the displacement magnitude at the incus to that at the umbo.

Figure 4 shows the ratios of the vibration magnitudes at the incus to those at the umbo as functions of frequency for the initial set of 1000 simulations. Each curve corresponds to an individual simulation with different model parameter values. To clearly show the shapes of some individual curves, the lighter curves (red online) show 20 randomly selected curves. The rest of the 1000 curves are shown in black. Note that the vertical scales are different from panel to panel. We see that, in the normal and ISJ disarticulation cases, the frequency response is fairly constant at lower frequencies but increases at higher frequencies, while in the IMJ disarticulation cases there is the opposite trend. In the

https://doi.org/10.1121/10.0022051

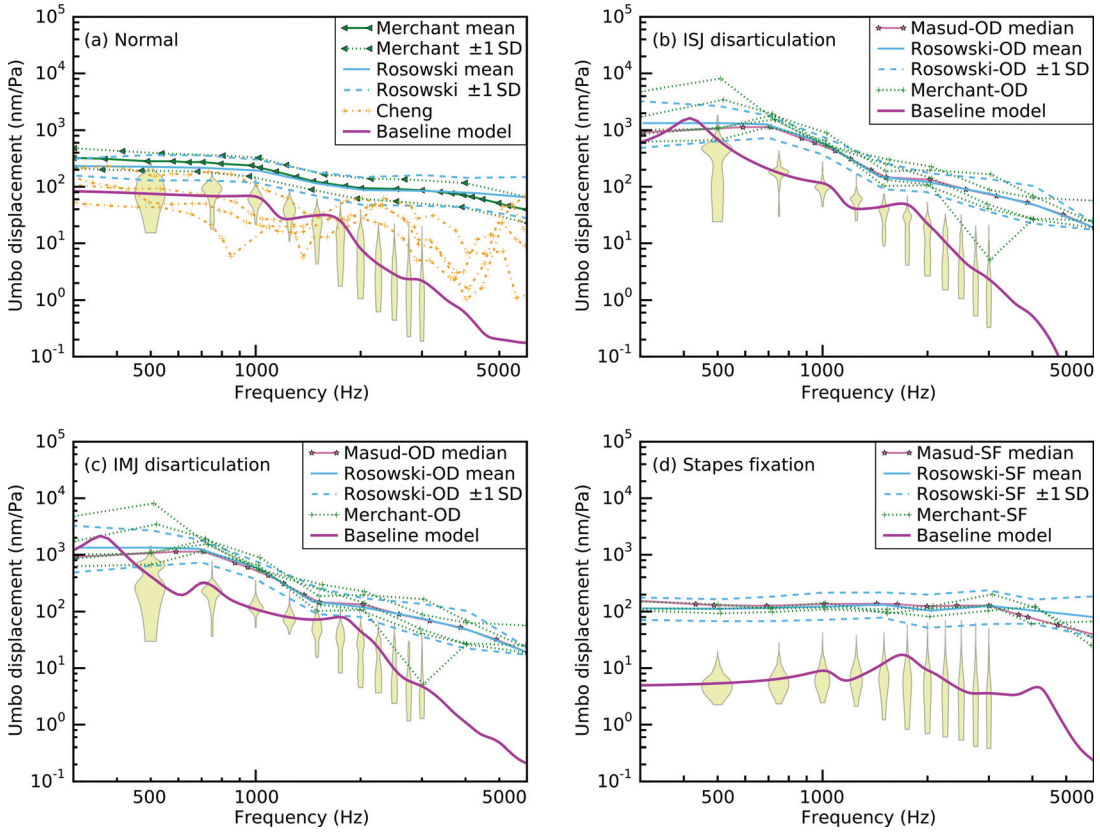

FIG. 2. Violin plots for the umbo displacement magnitudes (nm/Pa) for sets of 1000 simulations and curves for baseline models and from previous *in vivo* studies (Rosowski *et al.*, 2012; Merchant, 2014; Masud, 2020) and from the temporal-bone study of Cheng *et al.* (2021). (a) Normal, (b) ISJ disarticulation, (c) IMJ disarticulation, (d) stapes fixation.

stapes fixation cases, the curves are more flat and more or less independent of frequency. The ratio of incus displacement to umbo displacement was always less than 1 in the normal-ear OCT measurements of Golabbakhsh *et al.* (2023). However, we see in Fig. 4(a) that sometimes the simulated ratio is greater than 1. This is relatively rare for frequencies up to 2000, which was the highest frequency of the normal-ear OCT measurements in Golabbakhsh *et al.* (2023), but it happens more often at higher frequencies as the ossicular motions become more complicated (e.g., Decraemer and Khanna, 2004).

Figure 5 shows violin plots for the results in Fig. 4. We see that the value of the ratio is below 0.3 for the stapes fixation simulations at all frequencies and is always below 0.01 for the IMJ disarticulation simulations, while the ratio is always higher than 0.5 for the normal simulations and higher than 0.6 for the ISJ disarticulation simulations. We have used this fact in the first branch of the decision tree (Fig. 6), adopting a threshold value of 0.5, which classifies all of the samples correctly.

For distinguishing IMJ disarticulation from stapes fixation, we considered how the value of the ratio changes with frequency in the two cases. In the IMJ disarticulation simulations, the ratio is higher at lower frequencies (500 and 750 Hz) for about 85% of the curves, while in the stapes fixation simulations there was no definite trend across frequencies. Therefore, branch 2a of the decision tree was based on whether the ratio at 500 Hz is less than k_1 times the ratio at 3 kHz.

For distinguishing ISJ disarticulation from normal, we considered how the value of the umbo displacement changes with frequency in the two cases. In the ISJ disarticulation simulations, the umbo displacement was higher at 500 Hz than at 1 kHz while in normal simulations we did not find this trend. Therefore, branch 2b of the decision tree was based on whether the umbo displacement at 500 Hz is more than k_2 times the umbo displacement at 1 kHz.

A receiver operating characteristic (ROC) curve is a plot of a true positive rate (sensitivity) against a false positive rate (1 − specificity). It shows the performance of a binary classifier as its discrimination threshold is varied. Figure 7 shows the ROC curves for branches 2a and 2b of the decision tree, with triangles indicating selected values of k_1 between 0.8 and 10 and squares showing selected values of k_2 between 1.5 and 4. We defined the optimal point as the point minimizing the Euclidean distance between the ROC curve and the point (0,1) of the diagram. A value of $k_1 = 1.4$ was chosen, which gives a sensitivity of 0.904 and a specificity of 0.886 for branch 2a, and a value of $k_2 = 2.5$ was chosen, which gives a sensitivity of 0.787 and a specificity of 0.836 for branch 2b. We investigated the phase values and they did not appear to add information that would help to discriminate the conditions.

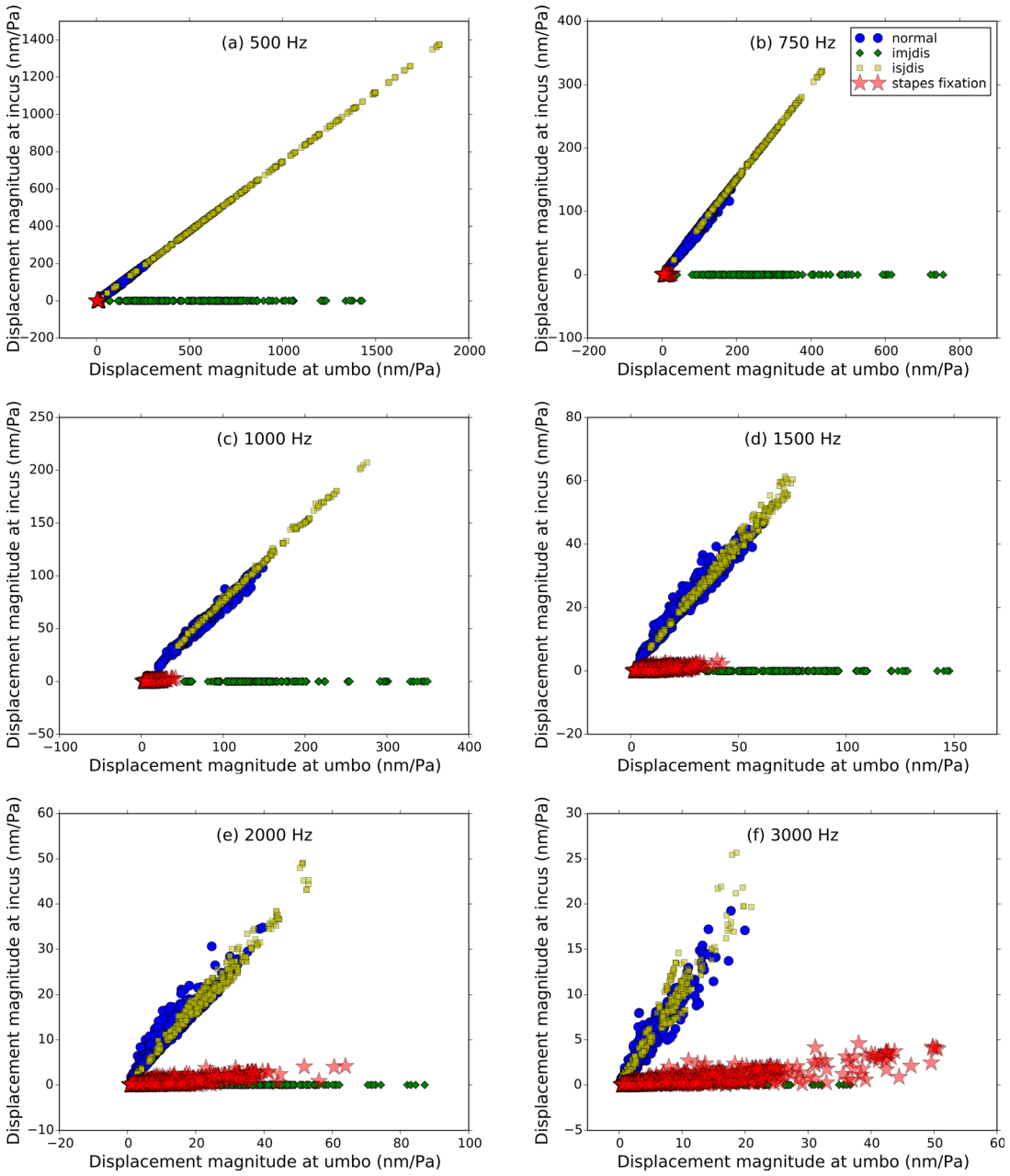

FIG. 3. (Color online) Incus vibration magnitudes vs umbo vibration magnitudes for simulated normal ears. Each panel shows 4000 simulation results (1000 simulations for each middle-ear case).

To validate the decision tree, we generated four more sets of 1000 simulations for each of the four conditions. We found that the sensitivity and specificity remained the same within ± 0.04 among the five sets, so we concluded that the decision tree could be based on the first set of 1000 simulations for each of the four conditions.

We tested the classifier for a set of 5000 additional simulations for each of the four conditions. The first branch of the decision tree again had a sensitivity and a specificity of 1, and we obtained a sensitivity = 0.900 and a specificity = 0.889 when distinguishing IMJ disarticulation from stapes fixation (Table II), within 0.004 of the initial results. We obtained a sensitivity = 0.784 and a specificity = 0.872 when distinguishing ISJ disarticulation from normal, within 0.04 of the initial results.

For the results so far, we have considered extreme pathological cases, with factors of zero for the joint disarticulations and 1000 for the stapes fixation. However, sometimes there may be a partial disarticulation or a partial fixation, and some patients with partial disarticulations are mistakenly diagnosed as having sensorineural hearing loss (Masud, 2020, p. 5). To see how the classifier works for a partial disarticulation of the IMJ, we simulated a set of 1000 ears with Young's modulus values different from zero for the IMJ: instead of using zero, the baseline value was divided by 1000. [By comparison, although Hirabayashi *et al.* (2022)

https://doi.org/10.1121/10.0022051

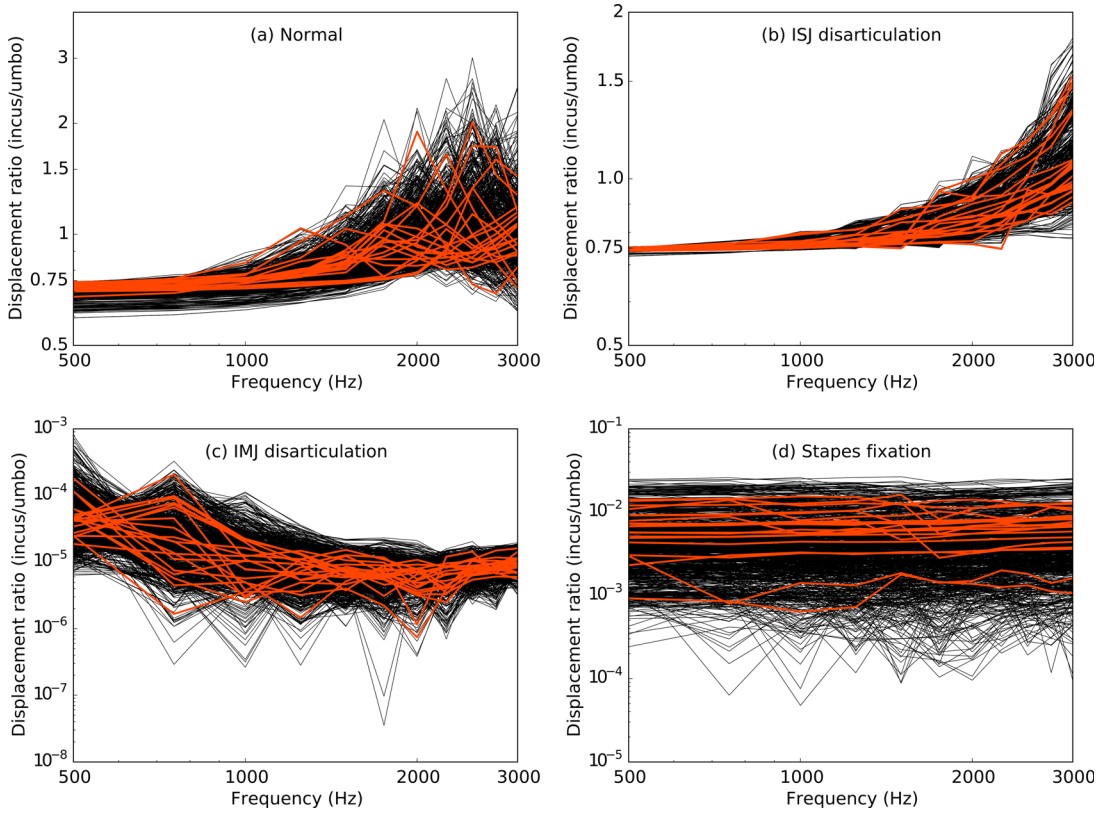

FIG. 4. (Color online) Ratio of displacement magnitude at the incus to that at the umbo, vs frequency, for the simulations of Fig. 3.

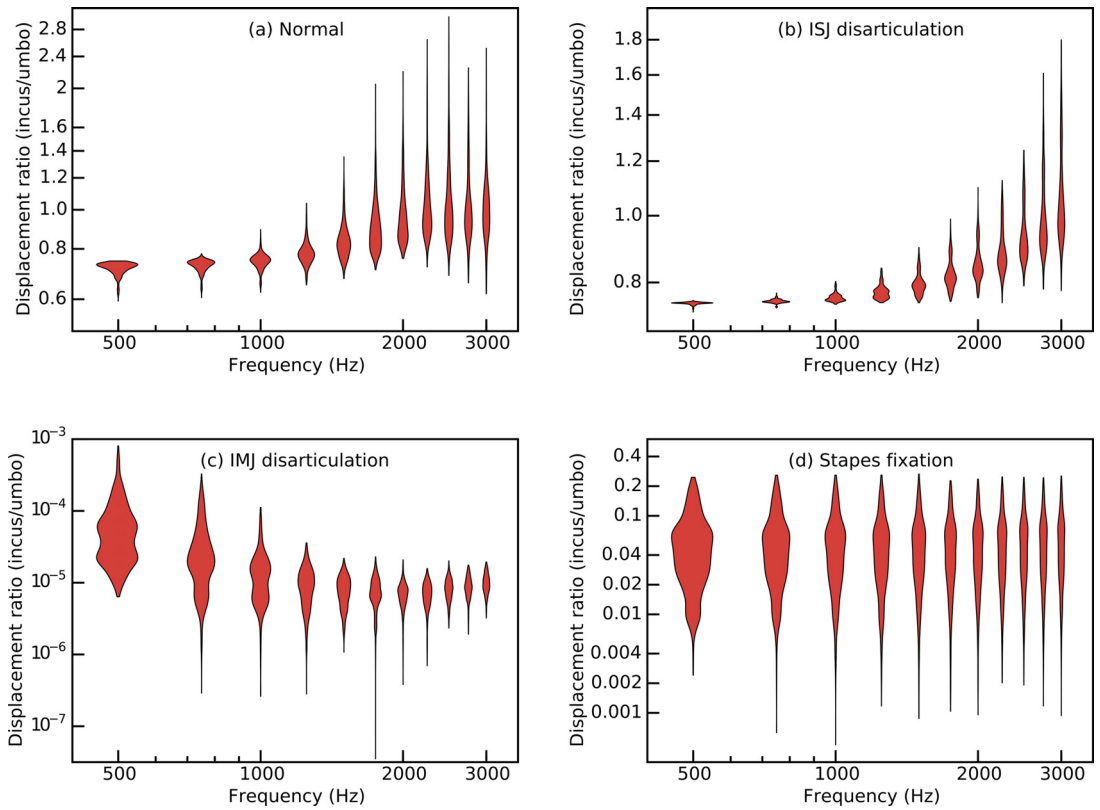

FIG. 5. (Color online) Violin plots of ratio of displacement magnitude at the incus to that at the umbo, at multiple frequencies, for the simulations of Fig. 4. (a) Normal, (b) ISJ disarticulation, (c) IMJ disarticulation, (d) stapes fixation.

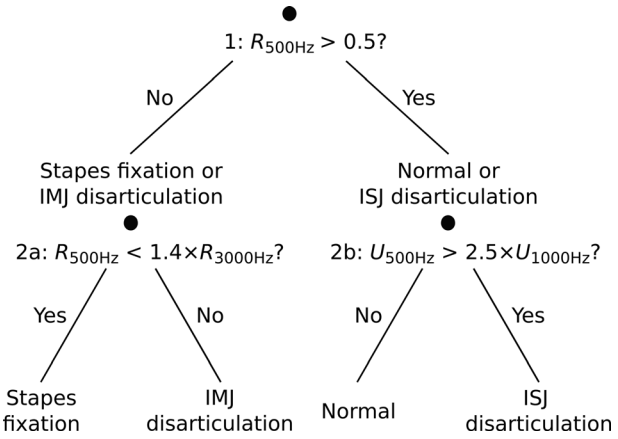

FIG. 6. Decision tree to distinguish between normal and pathological middle ears, R, ratio of displacement magnitude at the incus to that at the umbo; U, umbo displacement magnitude.

did not model IMJ disarticulation, for ISJ disarticulation, they used Young's moduli for the ISJ of 5, 10, 100, and 1000 times smaller than the value for the normal ear.] The same multipliers as for the extreme pathological cases (1.5 and 3) were applied to produce variability. We used the same k_1 value as for the extreme simulated pathologies to evaluate the performance of the classifier when there are different degrees of pathology that are not known *a priori*. Figure 8(b) shows the violin plots for the ratio of the vibration magnitude at the incus to that at the umbo for this set of 1000 simulations. For comparison, Fig. 8(a) shows the corresponding plots with the IMJ Young's modulus set to zero. Note that the range of the displacement scale in panel b is 500 times larger than that of panel a. While the heights of the violin plots get smaller with increasing frequency in panel a, the pattern is not so regular in panel b. Between 750–250 Hz, there are more cases higher than 0.5, but most

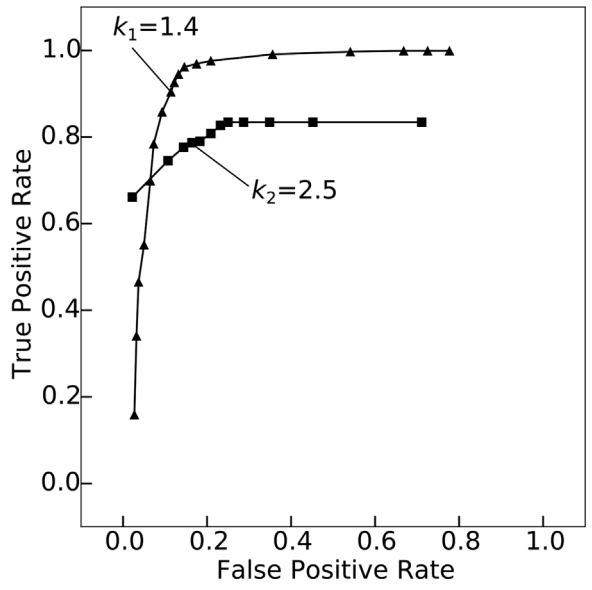

FIG. 7. Receiver operating characteristic (ROC) curves for the k_1 and k_2 thresholds at the second level of the decision tree.

TABLE II. Classification results for different conditions.

Condition	Sensitivity	Specificity
Extreme, branch 1	1.000	1.000
Extreme, branch 2a	0.900	0.889
Extreme, branch 2b	0.784	0.872
Partial IMJ disarticulation, branch1	1.000	0.926
Partial IMJ disarticulation, branch 2a	0.904	0.733
Partial stapes fixation, branch 1	1.000	0.932
Partial stapes fixation, branch 2a	0.996	0.886

of the cases are still below 0.5. The first level of the decision tree now gives a sensitivity of 1 and a specificity of 0.926 (compared to 1 and 1 when the IMJ Young's modulus = 0), while the second level now gives a sensitivity of 0.904 and a specificity of 0.733 (compared to 0.900 and 0.889 when the IMJ Young's modulus = 0).

We also simulated a set of ears with a less extreme stapes fixation, with the SAL stiffness taken to be 100 times that of the normal case, rather than 1000 times as was done above. [By comparison, for simulating stapes fixation, Hirabayashi *et al.* (2022) used Young's moduli for the SAL of 5, 10, 100, and 1000 times the value for the normal ear.] Figure 9(b) shows the violin plots for this case and we can see that the incus/umbo displacement ratio is larger than the previous results [Fig. 9(a)] by a factor of about 6. As the frequency increases, the displacement magnitudes increase and there are fewer outliers. The first level of the decision tree now gives a sensitivity of 1 and a specificity of 0.932 (compared with 1 and 1 before) while the second level gives a sensitivity of 0.996 and specificity of 0.886 (compared with 0.900 and 0.889 before).

We did not simulate ears with partial ISJ disarticulation, because the sensitivity and specificity values for distinguishing between extreme ISJ disarticulation and the normal case were already below 0.9.

For the partial IMJ disarticulation and the partial stapes fixation, for the second level of the decision tree, the specificity decreases by 0.156 and 0.003, respectively. The sensitivity, however, increases, by only about 0.004 for partial IMJ disarticulation but by 0.096 for stapes fixation. The relatively higher sensitivity for partial stapes fixation is because the frequency response of the partial stapes fixation rises at higher frequencies and better fits our decision criterion that the ratio at 500 Hz is smaller than $k_1 = 1.4$ times the ratio at 3000 Hz.

IV. DISCUSSION

We have explored using simulations of OCT vibration measurements at the umbo and incus in a decision tree to aid in distinguishing among normal and pathological conditions in the middle ear. In general, we aimed for a minimal set of features for classification. For one thing, we wanted to reduce the data-acquisition requirements and the computational cost if the classifier was used clinically. For another thing, we wanted a method that is easy to explain to

https://doi.org/10.1121/10.0022051

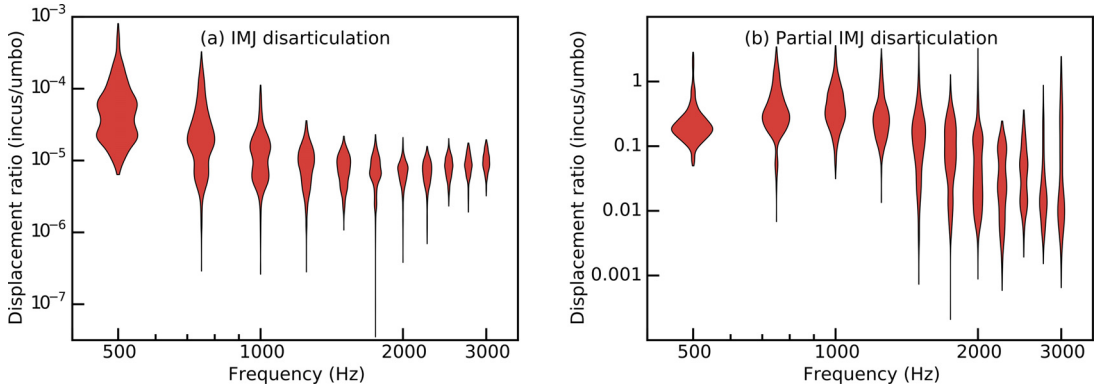

FIG. 8. (Color online) Violin plots of the ratio of displacement magnitude at the incus to that at the umbo, at multiple frequencies. (a) Extreme IMJ disarticulation, (b) partial IMJ disarticulation.

clinicians, to encourage its use in clinical decision making. Decision trees provide a simple and transparent model and are not computationally expensive. They can analyze a large amount of data quickly and help in efficient and accurate clinical decision making. In a previous application to the middle ear, Masud (2020, Chap. 4) used a decision tree to classify normal, ossicular discontinuity and stapes fixation based on measurements of wideband acoustic immitance and the air–bone gap (ABG) in patients.

We found potential discriminants for the purpose of distinguishing among simulated normal ears and ears with simulated stapes fixation and ossicular joint disarticulation. Finding the best discriminants based on simulation results will help future experimental and clinical researchers to decide what might be the most important measurement quantities, locations, and frequencies. Since only a limited number of frequencies can be tested clinically using OCT due to time limitations, in this work we wanted to identify a few frequencies that could best discriminate among the different conditions. Based on our results so far, we suggest that recording of the umbo and incus vibrations be conducted at both low and mid frequencies (e.g., 500 Hz and 3 kHz) to distinguish among the disorders considered here. We have presented simulation results up to 6 kHz in Fig. 2 but we have focused on frequencies only up to 3 kHz because our existing OCT data were limited to low frequencies. This limitation was a result of noise from fans in the laser unit in the current design, and we expect that subsequent designs will be able to reach much higher frequencies, as has been done by other groups (e.g., Kim *et al.*, 2019). The use of higher frequencies should provide additional information to aid in diagnosis, complicated by the fact that the 3D motions of the ossicles become more complex at high frequencies and OCT currently measures only the vibration component in the direction of the laser beam (which is approximately parallel to the axis of the ear canal and to the piston direction of the stapes).

So far, we have not considered the actual prevalences of the clinical pathologies in calculating the sensitivity and specificity. In addition, we have assigned the same relative cost to false positives and false negatives when choosing the threshold based on the ROC curve.

Our models were based on OCT measurements in cadaver ears, while clinical OCT measurements will obviously be performed *in vivo*. The TM and the middle ear as a whole are known to get stiffer *post mortem* as they dry (e.g., Kirikae, 1960, p. 47; Ellaham, 2007, p. 29). On the other hand, Rosowski *et al.* (1990, Table I and Fig. 10) found that, for 12 of their 15 cadaver ears, the acoustic input impedance varied by a factor of 2.6 and the range was almost the same as in earlier measurements in living ears. (In the other three cadaver ears, the impedance was beyond that range by a

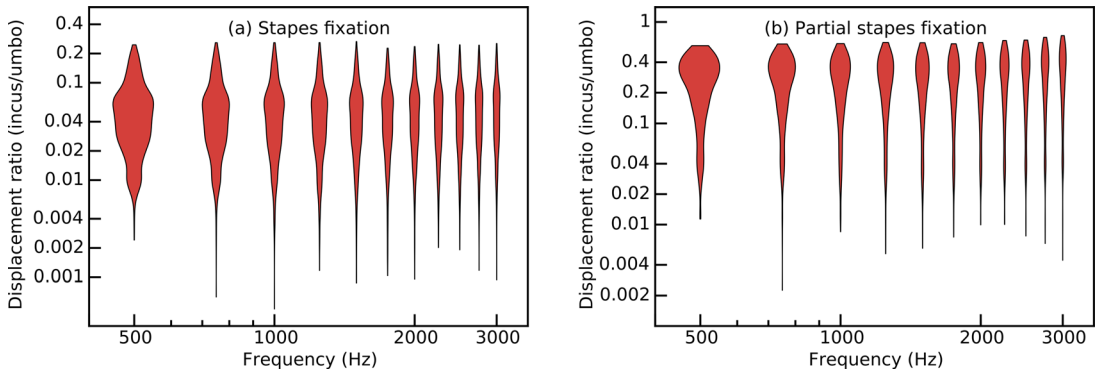

FIG. 9. (Color online) Violin plots of ratio of displacement magnitude at the incus to that at the umbo, at multiple frequencies. (a) Extreme stapes fixation, (b) partial stapes fixation.

factor of about 2.). Their 15 temporal bones were extracted "from refrigerated (3 °C) human cadavers within 48 h after death" and were either used "immediately" or "wrapped in wet gauze and stored in a freezer at −10 °C to −15 °C"; during measurements, the middle ears were kept "moist" by "periodic" rinsing of the ear canal with saline and then using "gentle suction … to remove all excess fluid"; and the middle-ear air pressure was kept at ambient pressure. Also, Goode *et al.* (1993) reported seeing similar umbo displacements in cadaver ears and living ears: at 500 Hz, the displacements varied by factors of about 7 and 6, respectively, and the ranges were almost the same. Their 15 "fresh" temporal bones were extracted "within 48 h after death", kept in a merthiolate solution at 5 °C, and used "within 6 days after death" (Goode *et al.*, 1993). The temporal bones used in our study were fresh frozen, and Rosowski *et al.* (1990) found that freezing and thawing in three ears had an effect of generally less than 40% on the impedance below 1 kHz and up to a factor of about 5 at frequencies beyond 1 kHz in two ears; the other ear had small changes at all frequencies.

Merchant (2014) and Masud (2020) did not separate ISJ and IMJ disarticulations, and instead just used ossicular discontinuity as a single category. It is important to distinguish them because the treatments will be different (e.g., what kind of implant will be used) and we analyzed them separately. To improve the classification results, it may be necessary to include data from clinical tests like the ABG, and possibly data from the medical history, along with the vibration measurements. It might also be useful to use the improvement of hearing after the Valsalva manoeuvre, which has been reported to be related to ISJ disarticulation (Sim *et al.*, 2013). Synthetic clinical data could be generated to supplement the synthetic vibration data to test this approach, as done by Hirabayashi *et al.* (2022) for the ABG, for example.

Masud (2020, Chap. 5) used the random-forest method to detect superior canal dehiscence. They suggested that the method could reach a higher sensitivity and specificity than Merchant *et al.* (2015) obtained using a decision tree for detecting this disorder. This was because Merchant *et al.* also had a problem with overfitting and the random-forest method helps to avoid overfitting by combining the predictions of an ensemble of decision trees. Supervised learning methods, such as *k*-nearest neighbours, support vector machines and neural networks, which work more automatically, can also be investigated. The discriminants identified by these more sophisticated methods may not have a straightforward physiological relevance to a pathology, and they thus may make discussions about differences among the disorders difficult. However, they might help with improving our performance in detecting ISJ disarticulation. If *in vivo* human OCT measurements can provide stapes displacements in the future, this would be helpful in better distinguishing ISJ disarticulation from the normal case. For example, in a study on cadaver chinchillas, Chang *et al.* (2013) were able to distinguish ISJ disarticulation from the normal case using OCT measurements of umbo, incus, and stapes.

It is difficult to know what values of stiffness to use for the IMJ, ISJ, and SAL to represent ears with hearing disorders. We initially selected the parameters related to each pathology following Sackmann *et al.* (2022), and then also looked at the effects of using less extreme values. The ranges of normal values for the stiffnesses of the ligaments are uncertain. For example, SAL stiffness values have varied by a factor of 10 across different studies, as discussed by Motallebzadeh *et al.* (2017). Our choice of values is supported by the fact that the umbo displacement changes for our simulated pathologies matched the experimentally measured changes. Hirabayashi *et al.* (2022) used values of 5, 10, 100, and 1000 times the normal case for the SAL, and showed that stiffnesses of 100 and 1000 times normal gave ABG results similar to measurements from patients [their Fig. 4(a)], consistent with our values. If OCT vibrometry were used to gather umbo and incus displacement measurements from subjects with different degrees of hearing loss and surgically confirmed diagnoses, it would be possible to use parameter fitting to build pathological models (e.g., using a pattern-search algorithm like that of Sackmann *et al.*, 2022) to match those data. Then, it would be possible to develop a classifier based on the models with those fitted parameters. In Golabbakhsh *et al.* (2023), we performed a typical one-at-a-time parameter-sensitivity analysis, but a global sensitivity analysis (e.g., Ebrahimian *et al.*, 2023a) would give additional insight into which parameters would most need to be included in the computationally expensive parameter fitting.

We have not considered modelling two pathologies present at the same time. It might be interesting to investigate that in the future. There are also additional pathologies that could be simulated, such as malleus fixation, incus fixation, ossicular erosion, and sclerosis of the ossicular ligaments (e.g., Daniel *et al.*, 2001).

In this work, we have used computational models to simulate the utilization of incus vibration measurements to classify the behaviour of normal and pathological middle ears. The results suggest that the vibration measurements beyond the TM that can be provided by OCT may provide a diagnostic method that is less invasive, less costly, and faster than surgery; and that is more accurate than just using immittance or LDV measurements, since neither one can measure incus vibrations in patients, while OCT can.

ACKNOWLEDGMENTS

This work was supported in part by the Canadian Institutes of Health Research, the Natural Sciences and Engineering Research Council of Canada, and the Faculty of Medicine and Health Sciences of McGill University. We are grateful for the help in using Narval that was provided by Calcul Québec and the Digital Research Alliance of Canada.

Chang, E. W., Cheng, J. T., Röösli, C., Kobler, J. B., Rosowski, J. J., and Yun, S. H. (**2013**). "Simultaneous 3D imaging of sound-induced motions of the tympanic membrane and middle ear ossicles," Hear. Res. **304**, 49–56.

Cheng, J. T., Ghanad, I., Remenschneider, A., and Rosowski, J. J. (**2021**). "The onset of nonlinear growth of middle-ear responses to high intensity sounds," Hear. Res. **405**(108242), 108242.
Dai, C., Cheng, T., Wood, M. W., and Gan, R. Z. (**2007**). "Fixation and detachment of superior and anterior malleolar ligaments in human middle ear: Experiment and modeling," Hear. Res. **230**, 24–33.
Daniel, S. J., Funnell, W. R. J., Zeitouni, A. G., Schloss, M. D., and Rappaport, J. (**2001**). "Clinical applications of a finite-element model of the human middle ear," J. Otolaryngol. **30**, 340–346.
Decraemer, W. F., and Khanna, S. M. (**2004**). "Measurement, visualization and quantitative analysis of complete three-dimensional kinematical data sets of human and cat middle ear," Middle Ear Mechanics in Research and Otology, pp. 3–10.
Dolbeau, R. (**2018**). "Theoretical peak FLOPS per instruction set: A tutorial," J. Supercomput. **74**, 1341–1377.
Ebrahimian, A., Mohammadi, H., and Maftoon, N. (**2023a**). "Relative importance and interactions of parameters of finite-element models of human middle ear," J. Acoust. Soc. Am. **154**, 619–634.
Ebrahimian, A., Mohammadi, H., Rosowski, J. J., Cheng, J. T., and Maftoon, N. (**2023b**). "Inaccuracies of deterministic finite-element models of human middle ear revealed by stochastic modelling," Sci. Rep. **13**, 7329.
Ellaham, N. (**2007**). "An experimental study of middle-ear vibrations in gerbils," M.Eng. thesis, McGill University, Montréal, Québec, Canada.
Farahmand, R. B., Merchant, G. R., Lookabaugh, S. A., Röösli, C., Ulku, C. H., McKenna, M. J., de Venecia, R. K., Halpin, C. F., Rosowski, J. J., and Nakajima, H. H. (**2016**). "The audiometric and mechanical effects of partial ossicular discontinuity," Ear Hear. **37**, 206–215.
Funnell W. R. J., and Golabbakhsh, M. (**2022**). Supplementary files for Golabbakhsh *et al*. (2023). https://borealisdata.ca/dataset.xhtml?persistentId=doi:10.5683/SP3/8BEY4N (Last viewed December 31, 2022).
Geuzaine, C., and Remacle, J.-F. (**2009**). "Gmsh: A 3-D finite element mesh generator with built-in pre- and post-processing facilities," Int. J. Numer. Meth. Engng. **79**, 1309–1331.
Golabbakhsh, M., Wang, X., MacDougall, D., Farrell, J., Landry, T., Funnell, W. R. J., and Adamson, R. B. A. (**2023**). "Finite-element modelling based on optical coherence tomography and corresponding x-ray microCT data for three human middle ears," J. Assoc. Res. Otolaryngol. **24**, 339–363.
Goode, R. L., Ball, G., and Nishihara, S. (**1993**). "Measurement of umbo vibration in human subjects—Method and possible clinical applications," Am. J. Otol. **14**, 247–251.
Gundersen, T., and Høgmoen, K. (**1976**). "Holographic vibration analysis of the ossicular chain," Acta Oto-Laryngol. **82**, 16–25.
Hirabayashi, M., Kurihara, S., Ito, R., Kurashina, Y., Motegi, M., Okano, H. J., Yamamoto, Y., Kojima, H., and Asakura, T. (**2022**). "Combined analysis of finite element model and audiometry provides insights into the pathogenesis of conductive hearing loss," Front. Bioeng. Biotechnol. **10**, 967475.
Huber, A., Koike, T., Wada, H., Nandapalan, V., and Fisch, U. (**2003**). "Fixation of the anterior mallear ligament: Diagnosis and consequences for hearing results in stapes surgery," Ann. Otol. Rhinol. Laryngol. **112**, 348–355.
Kim, W., Kim, S., Huang, S., Oghalai, J. S., and Applegate, B. E. (**2019**). "Picometer scale vibrometry in the human middle ear using a surgical microscope based optical coherence tomography and vibrometry system," Biomed. Opt. Express **10**, 4395–4410.
Kirikae, I. (**1960**). *The Structure and Function of the Middle Ear* (University of Tokyo Press, Tokyo).
Kwacz, M., Rymuza, Z., Michałowski, M., and Wysocki, J. (**2015**). "Elastic properties of the annular ligament of the human stapes–AFM measurement," J. Assoc. Res. Otolaryngol. **16**, 433–446.
MacDougall, D., Morrison, L., Morrison, C., Morris, D. P., Bance, M., and Adamson, R. B. A. (**2019**). "Optical coherence tomography Doppler vibrometry measurement of stapes vibration in patients with stapes fixation and normal controls," Otol. Neurotol. **40**, e349–e355.
Maftoon, N., Funnell, W. R. J., Daniel, S. J., and Decraemer, W. F. (**2015**). "Finite-element modelling of the response of the gerbil middle ear to sound," J. Assoc. Res. Otolaryngol. **16**, 547–567.
Masud, S. F. (**2020**). "Diagnosis of mechanical ear pathologies using structure-based modeling and machine learning techniques," Ph.D. thesis, Harvard University, Cambridge, MA.
Merchant, G. R. (**2014**). "Functional measurements of ear pathology in patients and cadaveric preparations," Ph.D. thesis, Massachusetts Institute of Technology, Cambridge, MA.
Merchant, G. R., Röösli, C., Niesten, M. E. F., Hamade, M. A., Lee, D. J., McKinnon, M. L., Ulku, C. H., Rosowski, J. J., Merchant, S. N., and Nakajima, H. H. (**2015**). "Power reflectance as a screening tool for the diagnosis of superior semicircular canal dehiscence," Otol. Neurotol. **36**, 172–177.
Motallebzadeh, H., Maftoon, N., Pitaro, J., Funnell, W. R. J., and Daniel, S. J. (**2017**). "Finite-element modelling of the acoustic input admittance of the newborn ear canal and middle ear," J. Assoc. Res. Otolaryngol. **18**, 25–48.
Park, J., Carbajal, E. F., Chen, X., Oghalai, J. S., and Applegate, B. E. (**2014**). "Phase-sensitive optical coherence tomography using an Vernier-tuned distributed Bragg reflector swept laser in the mouse middle ear," Opt. Lett. **39**, 6233–6236.
Ramier, A., Rosowski, J. J., and Yun, S.-H. (**2018**). "Optical coherence tomography for imaging the middle and inner ears: A technical review," in *13th Mechanics of Hearing Workshop: To the Ear and Back Again - Advances in Auditory Biophysics*, St. Catharines, Canada, p. 020001.
Rosowski, J. J., Davis, P. J., Merchant, S. N., Donahue, K. M., and Coltrera, M. D. (**1990**). "Cadaver middle ears as models for living ears: Comparisons of middle ear input immittance," Ann. Otol. Rhinol. Laryngol. **99**, 403–412.
Rosowski, J. J., Nakajima, H. H., Hamade, M. A., Mahfoud, L., Merchant, G. R., Halpin, C. F., and Merchant, S. N. (**2012**). "Ear-canal reflectance, umbo velocity, and tympanometry in normal-hearing adults," Ear Hear. **33**, 19–34.
Sackmann, B., Eberhard, P., and Lauxmann, M. (**2022**). "Parameter identification from normal and pathological middle ears using a tailored parameter identification algorithm," J. Biomech. Eng. **144**, 031006.
Sim, J. H., Huber, A. M., Häfliger, M., de Trey, L. A., Eiber, A., and Röösli, C. (**2013**). "Can an incomplete ossicular discontinuity be predicted by audiometric and clinical findings?," Otol. Neurotol. **34**, 699–704.
World Health Organization (**2021**). "World report on hearing," https://www.who.int/publications-detail-redirect/9789240020481 (Last viewed October 19, 2023).